Bioactive Materials 37 (2024) 72–85

Contents lists available at ScienceDirect

Bioactive Materials

journal homepage: www.keaipublishing.com/en/journals/bioactive-materials

Effects of MgO nanoparticle addition on the mechanical properties, degradation properties, antibacterial properties and in vitro and in vivo biological properties of 3D-printed Zn scaffolds

Leiting Yu [a], Fengdong Sun [a], Yuanyuan Wang [b], Wei Li [a], Yufeng Zheng [c], Guangxin Shen [d], Yao Wang [b,**], Minfang Chen [a,e,*]

[a] School of Materials Science and Engineering, Tianjin University of Technology, Tianjin, 300384, China
[b] School of Stomatology, Tianjin Medical University, Tianjin, 300070, China
[c] School of Materials Science and Engineering, Peking University, Beijing, 100871, China
[d] Changzhi Medical College, Changzhi, 046000, Shanxi, China
[e] National Demonstration Center for Experimental Function Materials Education, Tianjin University of Technology, Tianjin, 300384, China

ARTICLE INFO

Keywords:
3D printing
Porous
Skeletal–gyroid
Zn/MgO scaffold
Biocompatibility

ABSTRACT

Bone tissue engineering is the main method for repairing large segment bone defects. In this study, a layer of bioactive MgO nanoparticles was wrapped on the surface of spherical Zn powders, which allowed the MgO nanoparticles to be incorporated into 3D-printed Zn matrix and improved the biodegradation and biocompatibility of the Zn matrix. The results showed that porous pure Zn scaffolds and Zn/MgO scaffolds with skeletal-gyroid (G) model structure were successfully prepared by selective laser melting (SLM). The average porosity of two porous scaffolds was 59.3 and 60.0%, respectively. The pores were uniformly distributed with an average pore size of 558.6–569.3 μm. MgO nanoparticles regulated the corrosion rate of scaffolds, resulting in a more uniform corrosion degradation behavior of the Zn/MgO scaffolds in simulated body fluid solution. The degradation ratio of Zn/MgO composite scaffolds in vivo was increased compared to pure Zn scaffolds, reaching 15.6% at 12 weeks. The yield strength (10.8 ± 2.4 MPa) of the Zn/MgO composite scaffold was comparable to that of cancellous bone, and the antimicrobial rate were higher than 99%. The Zn/MgO composite scaffolds could better guide bone tissue regeneration in rat cranial bone repair experiments (completely filling the scaffolds at 12 weeks). Therefore, porous Zn/MgO scaffolds with G-model structure prepared with SLM are a promising biodegradable bone tissue engineering scaffold.

1. Introduction

The treatment of large segment bone defects requires suitable bone replacement materials, which should have good biocompatibility and mechanical properties, as well as appropriate biodegradability. In recent years, biodegradable metal materials have attracted much attention as materials for repairing large segment bone defects due to their excellent mechanical properties [1]. Degradable metal materials mainly include Mg, Zn and Fe. Since 2010, applications of biodegradable zinc (Zn) and Zn alloys have attracted attention [2,3]. As a universal trace element in the human diet and the second most abundant transition metal element in the human body, Zn plays a crucial role in the immune and nervous systems [4,5]. Moreover, Zn is an essential trace element and a cofactor of many enzymes and plays a crucial role in regulating the formation of proteins and nucleic acids [6,7]. Zn has a standard electrode potential of −0.76 V, intermediate between those of Fe (−0.44 V) and Mg (−2.38 V) [8], so Zn-based materials exhibit moderate degradation rates compared to Mg-based and Fe-based materials. The degradation products of Zn are biocompatible and can perform biological functions in the human body. In addition, Zn degrades into Zn^{2+}, and ionic Zn is also known as the "calcium of the 21st century" [9] because of the growing awareness of its important functional role in physiological and biological systems [10].

Peer review under responsibility of KeAi Communications Co., Ltd.
* Corresponding author. School of Materials Science and Engineering, Tianjin University of Technology, Tianjin 300384, China.
** Corresponding author. School of Stomatology, Tianjin Medical University, Tianjin, 300070, China.
E-mail addresses: wangyao1125@tmu.edu.cn (Y. Wang), mfchentj@tjut.edu.cn (M. Chen).

https://doi.org/10.1016/j.bioactmat.2024.03.016
Received 19 September 2023; Received in revised form 29 February 2024; Accepted 11 March 2024

Compared with the rate of bone repair, the degradation rate of Zn is still slow, so porous Zn scaffolds more easily to match the necessary degradation rate of biodegradable implants for clinical purposes [11,12]. The scaffold can greatly increase the contact area between the material and body fluid, effectively promote the transport of nutrients and the growth of bone tissue, and achieve a better degradation rate for degradable implants. However, the biocompatibility of Zn is not high enough, and the bone-promoting activity is significantly lower than that of Mg and its alloys, so researchers have made many attempts to improve the biocompatibility of Zn alloys. Mg is considered a functional element with good biosafety that can promote bone regeneration by inducing neurons to produce the calcitonin gene and related peptides [13]. Therefore, the addition of Mg to Zn alloys can improve the cytocompatibility of Zn alloys [14,15] and enhance the healing process of bone [16,17]. Tang et al. [14] studied the biocompatibility of Zn–Cu alloys with different Mg contents and found that the biocompatibility of Zn–Cu-xMg (x = 0, 0.1, 0.5 and 1.0 wt.%) alloys increased with the addition of Mg. Li et al. [15] studied the biocompatibility of Zn–1Mg binary alloy, and the results showed that compared with pure Zn and the negative control group, Zn–1Mg alloy significantly improved the activity of MG63 cells and promoted their proliferation. In addition, uneven degradation patterns of Zn-based materials in the physiological environment may lead to premature loss of mechanical integrity, high local ion concentrations, inflammation, and even implant material failure [18]. Therefore, a key aspect of research on biodegradable Zn materials is to change their degradation mode from inhomogeneous to uniform [19,20].

Bioactive ceramics have been widely used in bone repair materials because of their good bioactivity. For instance, Khalajabadi et al. [21] improved the bio-corrosion properties of a Mg/HA-based composite by the addition of various amounts of HA and periclase MgO nanoparticles. Sahmani et al. [22] significantly improved the mechanical properties and bioactivity of HA-MgO composite scaffolds by adding different weight fractions of MgO nanoparticles. In addition, the combination of biodegradable metals and bioactive ceramics has become a new idea to develop bone repair materials with both mechanical and biological activities. For example, the addition of bioactive ceramics such as hydroxyapatite (HA) and tricalcium phosphate (TCP) to Zn alloy as reinforcement can not only further regulate the mechanical properties of Zn alloy but also improve the osteogenic activity of the composite material, resulting in a bone repair composite material with potential worth researching. Yao et al. [23] prepared biodegradable Zn-1 wt.% Mg-n vol. % β-TCP (n = 0, 1, 3, 5, 10) composites by the hot-pressing sintering method. The degradation rate and cytocompatibility of the composites increased with increasing β-TCP content. Pan et al. [24] and Lu et al. [25] prepared Zn–1Mg-xTCP (x-0,1,3,5 vol.%) composite materials by casting. The research results showed that the biocompatibility and mechanical properties of the Zn–1Mg-1 vol.% β-TCP composite material are superior to those of the Zn–1Mg alloy. In addition, MgO as a bioactive ceramic reinforcement can significantly enhance the mechanical properties and corrosion resistance of Mg alloys. MgO can also be completely degraded to produce the same product as Mg in vivo [26]. Mg^{2+} will be produced after MgO degradation, which can promote the induction of bone formation. Tang et al. [27] added 0.3 wt.% MgO particles to Mg–3Zn-0.2Ca alloy, and the results indicated that the mechanical properties, corrosion resistance and cytocompatibility of Mg–3Zn-0.2Ca/0.3 wt.% MgO composites were superior to those of Mg–3Zn-0.2Ca alloy. Goh et al. [28] added MgO particles with different contents (0, 0.5, 0.75, 1.0 vol.%) to pure Mg, indicating that MgO nanoparticles can significantly enhance the hardness, yield strength and ultimate tensile strength of Mg materials. Khalajabadi et al. [29] prepared Mg-HA-MgO composites by powder metallurgy technology. The addition of MgO nanoparticles significantly reduced the porosity around the HA aggregates and ultimately improved the ductility and corrosion resistance of Mg/HA composites. In addition, Lei et al. [26] found that the mechanical properties and corrosion resistance of Mg matrix composites were enhanced by adding MgO ceramics as reinforcement by in situ reactive sintering technology. The above methods achieved positive results, but they involved adding MgO nanoparticles to Mg alloys. There are few studies on the addition of MgO ceramic nanoparticles to Zn alloys. Kumar et al. [30] prepared Zn/MgO composites by powder metallurgy technology, and the results indicated that the addition of an appropriate amount of MgO nanoparticles can reduce the grain size and improve the hardness and corrosion resistance of the composites. However, the biological properties of Zn/MgO composites in vitro and in vivo have not been studied.

A triply periodic minimal surface (TPMS) function is a periodic surface function with zero mean curvature at any point on the surface [31], which has smooth surfaces and highly connected pores. The overall structure is precisely controlled by an implicit function, which is an excellent solution for designing and modeling porous structures. TPMS structures have advantages over conventional porous structures in terms of structural efficiency and are receiving increasing attention. Among them, the Gyroid model exhibits a topology similar to that of human bone trabeculae and has potential in orthopedic bone replacement [32]. Among the many TPMS designs, the Gyroid structure shows advantages in terms of mechanical properties and permeability.

This study was designed to wrap bioactive MgO nanoparticles on the surface of spherical Zn powder by ball milling treatment, so that they can be incorporated into the Zn matrix by laser melting during 3D printing. Due to the unmatched interfacial relationship between Zn matrix and MgO nanoparticles, the body fluid is more easily to penetrate through the micropores around the MgO nanoparticles during in vivo and in vitro corrosion, preferentially reacting with Cl^{-}, releasing Mg^{2+} and forming in-situ pores, which increases the bioactivity and osteogenic capacity of the composite, and accelerates the corrosion rate. This is the innovation of this research work, which provides a new idea for the application of Zn and its alloy scaffolds in the field of bone tissue engineering.

2. Materials and methods

2.1. Mixing and characterization of Zn powder and MgO powder

Spherical Zn powder is from Hunan New Welllink Advanced Metallic Material Co., Ltd. MgO nanoparticles with an average particle size of 49.9 nm (as shown in Fig. S1) was manufactured by a hydrothermal method, which was also reported in the literature [33]. Spherical Zn powder and MgO nanoparticles were uniformly mixed by a ball mill (QM-3SP4). The ratio of spherical Zn powder to MgO nanoparticles was 499:1 mass percentage. One hundred grams of mixed powder was added to each ball mill tank, and approximately 12 mL of anhydrous ethanol was added to the mixed powder before ball milling to prevent oxidation of the Zn powder during the milling process. The frequency and time of ball milling are set to ensure that the spherical Zn powder and MgO nanoparticles were fully and evenly mixed and to prevent the sphericity of the spherical Zn powder from being damaged.

2.2. Preparation for 3D-printed pure Zn and Zn/MgO composite scaffolds

The G model was designed by computer aided design (CAD) software, where the designed porosity is 76% and the monomer edge length is 1200 mm (corresponding pore size is 0.77 mm). The 3D model data saved in STL format were imported into the BLT-S200 series 3D metal printer (Xi'An Bright Laser Technologies Co., Ltd). Pure Zn scaffolds and Zn/MgO composite scaffolds were printed by pure Zn spherical powder and Zn matrix composite powder treated by ball milling, respectively. The laser scanning speed was 1100 mm/s, the laser power was 120 W, the powder laying method was one-way powder laying, and the single powder thickness was 0.02 mm. Argon gas was injected into the printing process for protection to eliminate the negative effects of evaporation and other harmful gases. The final cube of 9.6 mm × 9.6 mm × 9.6 mm

was prepared for in vitro experiments and in vivo implantation. After printing, the specimen was removed from the Zn substrate by wire-cutting and then ultrasonically cleaned with anhydrous alcohol to remove excess powder from the scaffold hole.

2.3. Morphological characterization of pure Zn and Zn/MgO composite scaffolds

The spherical Zn powder before and after ball milling was tested by scanning electron microscope (SEM, Quanta FEG 250, USA) to measure and calculate the average particle size of the spherical Zn particles and to observe whether the MgO nanoparticles were uniformly mixed with the spherical Zn powder after ball milling. The actual porosities of the pure Zn scaffold and Zn/MgO composite scaffold were measured by the mass method [34,35]. The actual pore sizes of the pure Zn scaffold and the Zn/MgO composite scaffold were measured and counted by Nano Measurer software. The microstructures of the pure Zn and Zn/MgO composite were observed by scanning electron microscope (SEM, Quanta FEG 250, USA), and the spherical Zn particles and MgO nanoparticles as well as the composition of the second phase were quantitatively analyzed by energy dispersive spectrometry (EDS, Quanta FEG 250, USA).

2.4. Mechanical tests

The dimensions of the compressed specimen were 9.6 mm × 9.6 mm × 9.6 mm. The compression test was carried out at room temperature with a universal testing machine (DDL50, China) with a compression speed of 0.5 mm/min. There were 3 parallel samples in each group. The quasielastic modulus [36] (referred to as the elastic modulus) was determined by the cross head displacement of the initial linear slope of each sample, and the yield strength was calculated by the 0.2% migration method [37]. A micro-Vickers hardness tester (HMV-2T) was used to test the hardness values of the pure Zn scaffold and the Zn/MgO composite scaffold.

2.5. In vitro degradation experiment

In vitro immersion tests were performed according to ASTM G31-2012a. The ratio of surface area between the immersed solution and the porous sample is 20 mL/cm^2 [38]. The porous pure Zn and Zn/MgO composite scaffold samples were immersed in simulated body fluid (SBF) at 37 °C for 30 days. During the test, the temperature was controlled at 37.0 ± 0.5 °C using a constant temperature oscillating water bath (WE-4, China). The SBF was updated every two days to simulate human circulation, bringing the solution close to the ion concentration in the body [39]. After immersion for 30 days, the samples were gently rinsed with anhydrous ethanol, dried at room temperature and stored under vacuum. The corrosion products of the samples were removed with chromic acid solution, dried and weighed. The corrosion rates (CR) of the samples on Days 10, 20, and 30 were calculated according to Formula (1):

$$CR = \frac{m_0 - m_1}{T} \quad (1)$$

where m_0 is the original mass of the sample, m_1 is the mass of the sample after removing the corrosion product, and T is 10 days, 20 days, and 30 days.

2.6. Antibacterial experiment

The antibacterial activity of the pure Zn scaffold and the Zn/MgO composite scaffold was evaluated against gram-positive *Staphylococcus aureus* (*S. aureus*) and gram-negative *Escherichia coli* (*E. coli*). Ten microliters of bacterial solution was placed in a test tube, and 1 mL of deionized water was added. The sample was also placed in the test tube and incubated together with the bacterial solution in a shaker at 37 °C for 24 h. Then, the incubated mixed solution was diluted 1 million times with deionized water, and 100 μL of the diluted mixed solution was dropped on an AGAR plate for spin coating. The AGAR plate was cultured in an incubator at 37 °C for 24 h. Finally, the AGAR plate was removed and photographed. To observe the morphologies of bacteria, the samples were fixed with 2.5 vol.% glutaraldehyde, immersed in anhydrous ethanol and tert-butanol solution, and then vacuum freeze-dried. The morphologies of the bacteria were observed under an ultrahigh-resolution scanning electron microscope (SEM, Verios 460 L, America). The antibacterial rates (AR) of the pure Zn scaffold and the Zn/MgO composite scaffold samples were calculated by Formula (2):

$$AR = \frac{NC_b - NC_e}{NC_b} \times 100\% \quad (2)$$

where NC_b is the number of colonies in the blank group and NC_e is the number of colonies in the experimental group.

2.7. Direct cell coculture experiment

MC-3T3 cells were cultured with α-MEM (containing 10% FBS, Gibco, 100 U/mL Pen and 100 μg Str. Genview) in a humid environment at 37 °C and 5% CO_2. The pure Zn scaffold and the Zn/MgO composite scaffold samples were sterilized by UV irradiation for 12 h on both sides prior to cell inoculation and then immersed in α-MEM at 37 °C for 3 days (pretreatment). After 3 days, the medium was removed, and MC-3T3 cells (2.0×10^4 cells/mL) were seeded on the surface of the pretreatment sample for 48 h and then washed with PBS solution three times and in 4% paraformaldehyde (PFA, AR-0211, China) for 30 min. The fixed cells were dehydrated by a gradient of ethanol solution with concentrations of 50%, 70%, 90% and 100% and then treated with gold spray after air drying. The morphologies and adhesion of the cells were observed by SEM. In addition, the untreated samples were directly rinsed twice with PBS and α-MEM and then observed for cell adhesion after the above cell coculture steps were used as controls. The cells of pretreated samples were treated with Triton X-10 (Dingguo, China). Subsequently, the F-actin and nuclei were stained with FITC (DH127-1, China) and DAPI (CAS#: 28718-90-3, Genview) and then observed with a confocal laser scanning microscope (Olympus FV1000, Japan).

2.8. In vivo skull repair experiment

Forty-five 8-week-old 250 g male SD rats were randomly divided into 3 groups (SD rats were provided by SPF (Beijing) Biotechnology Co., Ltd.). The following groups were set up: (1) blank group (the bone defect area was not filled with scaffolds), (2) Zn group (the bone defect area was filled with the pure Zn scaffold), and (3) Zn/MgO group (the bone defect area was filled with the Zn/MgO composite scaffold). Fig. S2 shows the establishment of the skull defect model and scaffold implantation operation in SD rats. Fasting and water abstinence were performed for 12 h before the operation, and the rats were given general anesthesia with 5% w/v chloral hydrate before the operation. A full-layer skull defect model with a diameter of 5 mm was made by using a trephine with a 5 mm outer diameter drilled into the left side of the sagittal suture of the skull with a low-speed drilling machine. Pure Zn scaffolds and Zn/MgO composite scaffolds of Φ5 × 1 mm were implanted, and the blank group was not treated. All rats were sutured. The samples were observed at 2, 4, 8 and 12 weeks after implantation. The heart, liver, spleen, lung, kidney and blood were taken under general anesthesia at 2, 4, 8 and 12 weeks. The SD rats were killed by an overdose of anesthesia, and their skulls were removed. After the internal organs were fixed, embedding, sectioning, and HE staining were performed to determine the toxicity of the different scaffolds to the internal organs in vivo. The skull was reconstructed with micro-CT (SkyScan1276 , Bruker), and a 3D model of the implanted scaffold was

constructed. The bone tissue at the scaffold site was fixed and dehydrated by an ethanol gradient. Then, the specimen was embedded in paraffin. After 3 weeks, the cured specimen was removed, and the hard tissue was sliced. Then Masson staining (Servicebio, Code: G1006) was utilized to observe the formation of new bone around the specimen with a microscope.

2.9. Statistical analysis

In this work, the results of in vivo biocompatibility experiments are presented as an average ± SD. Two-way ANOVA by GraphPad Prism software revealed significant differences between the data for different groups. $p < 0.05$ was considered to indicate statistical significance.

3. Results

3.1. Characterization of Zn–MgO mixed powder

Fig. 1a shows the SEM image of spherical Zn powder. It can be seen in Fig. 1a that the sphericity of the spherical Zn powder is high, and the size distribution is very uniform. The particle size of spherical Zn powder was calculated and is quantitatively presented in the form of a histogram in Fig. 1b. According to the particle size distribution in Fig. 1b, the average particle size of spherical Zn powder is 27.93 ± 0.76 μm, of which 10% is 16.58 μm, 50% is 25.77 μm, and 90% is 36.68 μm. Therefore, it meets the powder standards for normal selection laser melting.

Fig. S3 shows the mixed print powder after treatment with different mixing parameters. It can be seen that when the frequency was 15 Hz, the ball milling treatment for 15 min, 10 min and 5 min affected the sphericity the Zn powder due to the fast rotational speed. When the frequency was 10 Hz, the ball milling treatment for 15 min had a small effect on the sphericity of the Zn powder, and when the ball milling was done for 10 min, the sphericity of the ball milled powder was similar to the shape of the original spherical Zn powder. By adjusting the frequency and ball milling time through the ball mill, the optimum ball milling parameters were derived, i.e., when the frequency was 10 Hz and the ball milling time was 10 min, the sphericity of the printed powder could be maintained similar to that of the original spherical zinc powder. And this ball milling parameter was used to obtain the printing powder for 3D-printed Zn/MgO composite scaffolds. Fig. 1c–h indicate the EDS element mapping images of spherical Zn powder particles mixed with MgO nanoparticles. It is obvious from the EDS analysis that MgO nanoparticles are uniformly coated on the surface of spherical Zn powder particles after ball milling. There are Zn, Mg and O elements on the surface of spherical Zn powder particles (Fig. 1e), in which the percentage content of Mg and O elements is 20.12 at.% and 29.19 at.%, respectively, and the rest is Zn, accounting for 50.69 at.% of the percentage ratio. The content of O is approximately 9 at.% higher than that of Mg, indicating that slight oxidation (ZnO formation) occurs on the surface of zinc powder during the ball milling process.

3.2. Structure and mechanical properties of porous scaffolds

Fig. S4 shows the designed G model and Fig. 2a–b shows the printed scaffolds. The results elucidated the excellent printability and integrity of the pure Zn scaffolds and the Zn/MgO composite scaffolds without broken struts and interlayer delamination. From the microstructure of the Zn/MgO composite scaffolds shown in Fig. 2c, it can be seen that the MgO nanoparticles are aggregated into larger particles of 200–400 nm distributed at the grain boundaries of the Zn matrix. The EDS analyses confirm that point A and point B are Zn matrix and MgO particles, respectively. Although the L-PBF process provides extremely high temperatures and a strong Marangoni effect, some micropores are still observed the interface between the MgO nanoparticle and the Zn matrix, even among the MgO nanoparticles (as indicated by the red arrow in Fig. 2c). The actual porosity and pore size of the printed scaffolds are statistically shown in Fig. 2d. It was observed that the actual porosity of the Zn/MgO composite scaffold was 60.0 ± 1.2%, and that of the pure Zn scaffold was 59.3 ± 1.8%. In other words, the relative density of the

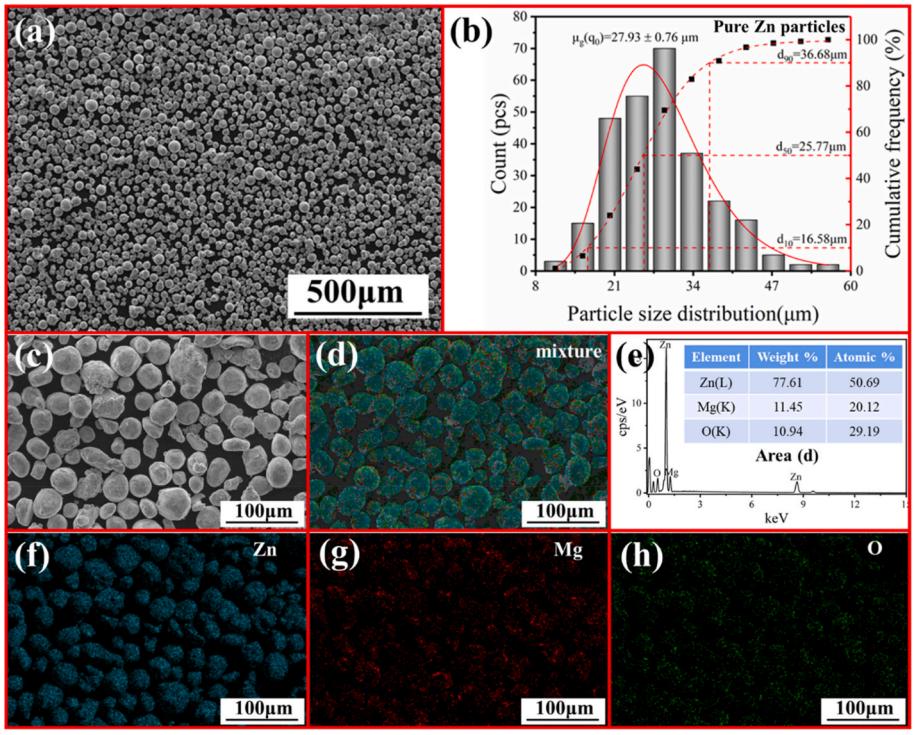

Fig. 1. (a–b) The SEM images and particle size distribution of spherical Zn powder, (c–h) the SEM images and EDS element mapping images of Zn–MgO mixed powders.

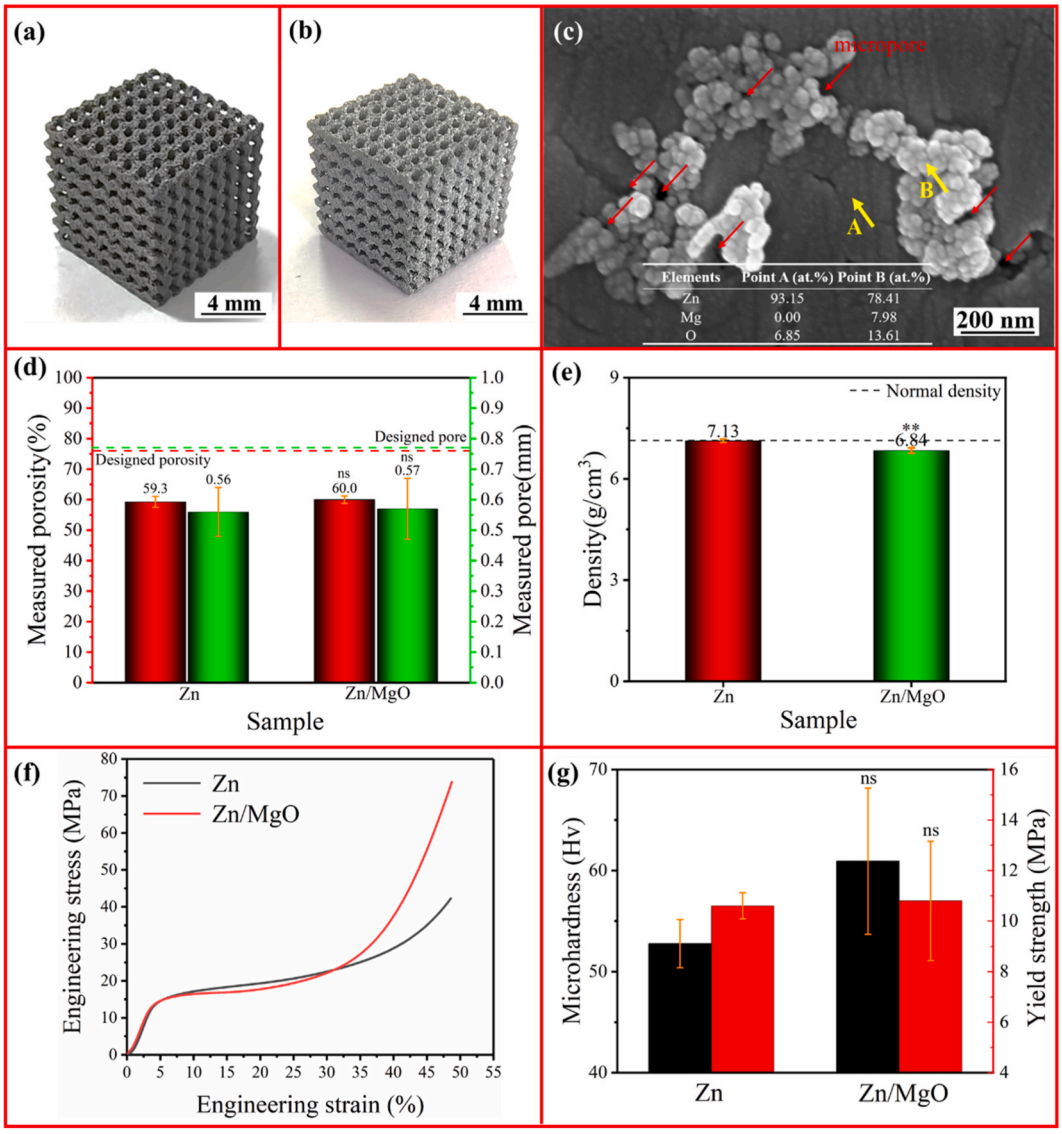

Fig. 2. Characterization and mechanical properties of the printed scaffolds. (a) The digital image of the pure Zn scaffold, (b) the digital image of the Zn/MgO composite scaffold, (c) the microstructure and the EDS analysis of the interface between the MgO and Zn matrix of Zn/MgO scaffolds, (d) the measured porosity and pore size of scaffolds, (e) the measured density of scaffolds, (f) compressive stress–strain curve, (g) yield strength and micro-Vickers hardness. (**$p < 0.01$, ns: $p > 0.05$).

Zn/MgO composite scaffold is slightly lower than that of the pure Zn scaffold, which is also confirmed in Fig. 2e. Furthermore, the presence of these micropores (in Fig. 2c) led to a lower actual measured density than the theoretical apparent density of the Zn/MgO composite scaffolds. Compared with the pure Zn scaffold, the porosity of the Zn/MgO composite scaffold is closer to the designed porosity (76%), and the pore size of the Zn/MgO composite scaffold is closer to the designed pore size (0.77 mm). This can be attributed to the increase in the size of the pillar measured by the experiment compared to the designed value [40]. The printing error of the Zn/MgO composite scaffold is smaller than that of the pure Zn scaffold. The reason may be that during the 3D printing process, the adhesion of the MgO nanoparticles on the surface of the spherical Zn powder prevents the adhesion of the melted Zn powder and the unmelted Zn powder. The existence of printing errors also indicates the shortcomings of 3D-printed Zn: the low melting point, high vapor pressure and oxidation sensitivity of Zn reduce printing accuracy [41].

Fig. 2f shows the compressive stress–strain curves of the pure Zn scaffold and the Zn/MgO composite scaffold. The scaffold exhibits stress–strain behavior typical of porous materials and reflects three states of cancellous bone, namely, the linear elastic region, plastic plateau region and densification region [42]. Fig. 2f indicates that the stress-strain curves of the pure Zn scaffold and the Zn/MgO composite scaffold show a similar trend. The elastic modulus of the pure Zn scaffold and the Zn/MgO composite scaffold was 0.323 ± 0.010 GPa and 0.365 ± 0.005 GPa, respectively. Fig. 2g shows the yield strength and Vickers hardness values of the pure Zn scaffold and the Zn/MgO composite scaffold. The Vickers hardness values of the pure Zn scaffold and the Zn/MgO composite scaffold were 52.78 ± 2.39 HV and 60.93 ± 7.22 HV, respectively. This indicates that the addition of MgO nanoparticles improves the hardness of printed pure Zn scaffolds. The yield strength of the pure Zn scaffold and the Zn/MgO composite scaffold was 10.6 ± 0.5 MPa and 10.8 ± 2.4 MPa, respectively. These values are within the typical compressive strength range of cancellous bone (0.1–16 MPa) [43,44]. In addition, Fig. 2f indicates that the distribution of stress and strain is uniform throughout the G model structure. When applied, the adhesive cells will be subjected to more equal stress stimulation throughout the structure, which may facilitate cell response to the matrix [45].

3.3. In vitro degradation behavior

To compare the degradation of the pure Zn scaffold and the Zn/MgO composite scaffold, the corrosion morphologies and degradation rates of the two scaffolds were observed. Fig. 3a–f shows the macroscopic morphologies of the corrosion products of the pure Zn scaffolds and the Zn/MgO composite scaffolds immersed in SBF solution for 10 days, 20 days and 30 days. As shown in Fig. 3a–f, the pure Zn scaffold corrodes from the vertex position first in SBF solution, and with the extension of immersion time, the corrosion products are deposited and gradually increase, so the corrosion products are concentrated in each vertex region of the scaffold. In contrast, the Zn/MgO composite scaffold preferentially corrodes from the surface of the sample in SBF solution, and with increasing time, the corrosion products also gradually increase. By the 30th day, the corrosion products are mostly deposited on certain outer surfaces of the scaffold. The scaffolds of the two materials exhibit different corrosion patterns. The pure Zn scaffold tended to exhibit pitting corrosion, while the Zn/MgO composite scaffolds tended to exhibit surface corrosion. The Zn/MgO composite scaffolds corroded more uniformly than the pure Zn scaffolds. Fig. 3g–h shows the macroscopic morphologies of the removal products of the pure Zn scaffolds and the Zn/MgO composite scaffolds after 30 days of immersion. From Fig. 3g–h, it can be seen that the pure Zn scaffold has some pitting pits after 30 days of degradation, indicating that it undergoes inhomogeneous pitting in SBF solution, resulting in a large corrosion rate for the pure Zn scaffolds. In contrast, the Zn/MgO composite scaffold shows structural integrity on the macroscopic level without obvious pitting pits at 30 days indicates that it undergoes more homogeneous corrosion in the SBF solution. The addition of MgO nanoparticles transforms the corrosion of Zn from pitting corrosion to more uniform corrosion, which also enables the Zn/MgO composite scaffolds to exhibit a long-term mechanical load-bearing effect throughout the implantation process. From the monitored pH during immersion in Fig. 3i, it can be seen that the pH of the Zn scaffolds showed a relatively uniform increase. Whereas the pH of the Zn/MgO scaffolds increased at a faster rate in the early stage, the rate slowed down by day 15 and was lower than the pH of the Zn scaffolds by day 26. Fig. 3j shows that the corrosion rates of the pure Zn scaffold immersed in SBF solution for 10 days, 20 days and 30 days are 1.8 mg/day, 3.7 mg/day and 4.6 mg/day, respectively, while those of the Zn/MgO composite scaffold are 2.3 mg/day, 2.9 mg/day and 2.3 mg/day, respectively. The corrosion rate of the pure Zn scaffold increases with time, whereas the corrosion rate of the Zn/MgO composite scaffold first increases and then decreases with time. Moreover, the average corrosion rate of Zn/MgO scaffolds was higher than that of Zn scaffolds during the first 10 days of degradation. The average degradation rate of Zn/MgO scaffolds slowed down by days 20 and 30. This indicated that the formed Ca–P products blocked the pores of the Zn/MgO scaffolds after 10 days, which led to a much lower corrosion rate being calculated at a later stage.

The microscopic corrosion morphology of the scaffolds is shown in Fig. S5, where the Zn scaffolds showed slatted corrosion products on the surface after 30 days of immersion with a few interspersed nano spherical particles. The Zn/MgO scaffolds were all characterized by denser submicron spherical particles on the surface. After EDS (Fig. S5e) analysis, the slatted corrosion products (Point A) were identified as ZnO and the spherical particles (Point B and C) were identified as Ca–P products. Thus, the degradation of Zn/MgO scaffolds is faster in the early stage and slower in the later stage. This is due to the fact that more

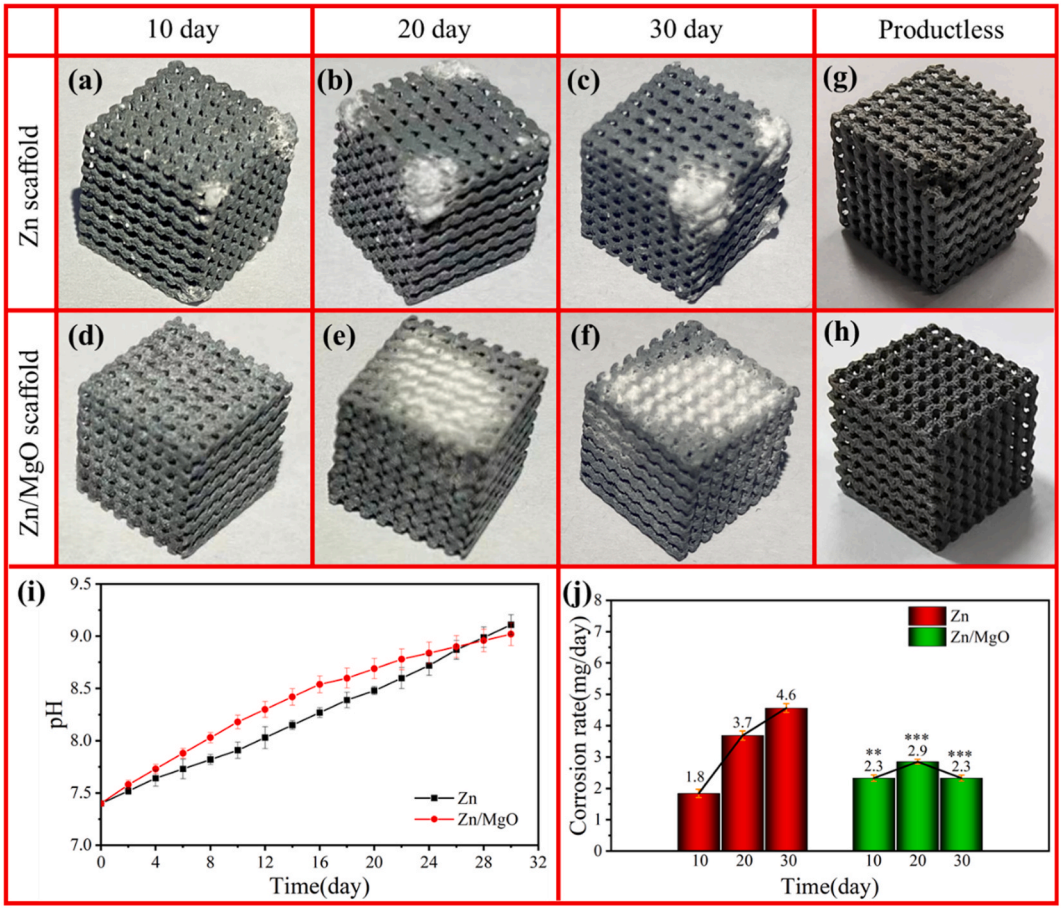

Fig. 3. In vitro degradation behavior of the scaffolds. (a–f) The digital images of the scaffolds with corrosion products, (g–h) the digital image of removal products after 30 days of immersion, (i) pH value of scaffolds during immersion, (j) corrosion rates after 10, 20, and 30 days of immersion.

Ca–P products are deposited on the surface of the Zn/MgO scaffolds, hindering the entry of body fluid into the interior of the scaffolds at later stages.

3.4. Antibacterial properties

As shown in Fig. 4a–f, the antibacterial susceptibility of the pure Zn scaffold and the Zn/MgO composite scaffold materials evaluated against *E. coli* and *S. aureus* were tested in AGAR plate medium. AGAR plate medium without either material was used as a blank control group. Fig. 4k-l shows the antibacterial rates of the two materials against different bacteria. The antibacterial rates of all samples reached more than 99%, except that the antibacterial rate of the pure Zn scaffold against *S. aureus* was 76%. The results showed that both the pure Zn scaffold and the Zn/MgO composite scaffold had good antibacterial effects, and the antibacterial activity of the Zn/MgO composite scaffold was higher than that of the pure Zn scaffold. The reason is that MgO nanoparticles can easily enter bacteria and provide a high surface area for interactions that hinder bacterial growth mechanisms [46,47]. In addition, MgO nanoparticles can induce lipid peroxidation of the bacterial membrane and destroy the peptide bond structure of the bacterial membrane, resulting in bacterial membrane damage and the leakage of substances in the bacteria, thereby rapidly killing them [48].

Fig. 4g–j shows the morphologies of *E. coli* and *S. aureus* on the surface of the pure Zn scaffold and the Zn/MgO composite scaffold after coculture with bacterial solution for 24 h. It was observed that only a small number of bacteria adhered to the surface of the pure Zn scaffold and the Zn/MgO composite scaffold, and both *E. coli* and *S. aureus* had irregular shapes and folded bacterial membranes. The results showed that both Zn^{2+} and MgO nanoparticles could inhibit bacterial adhesion and biofilm formation.

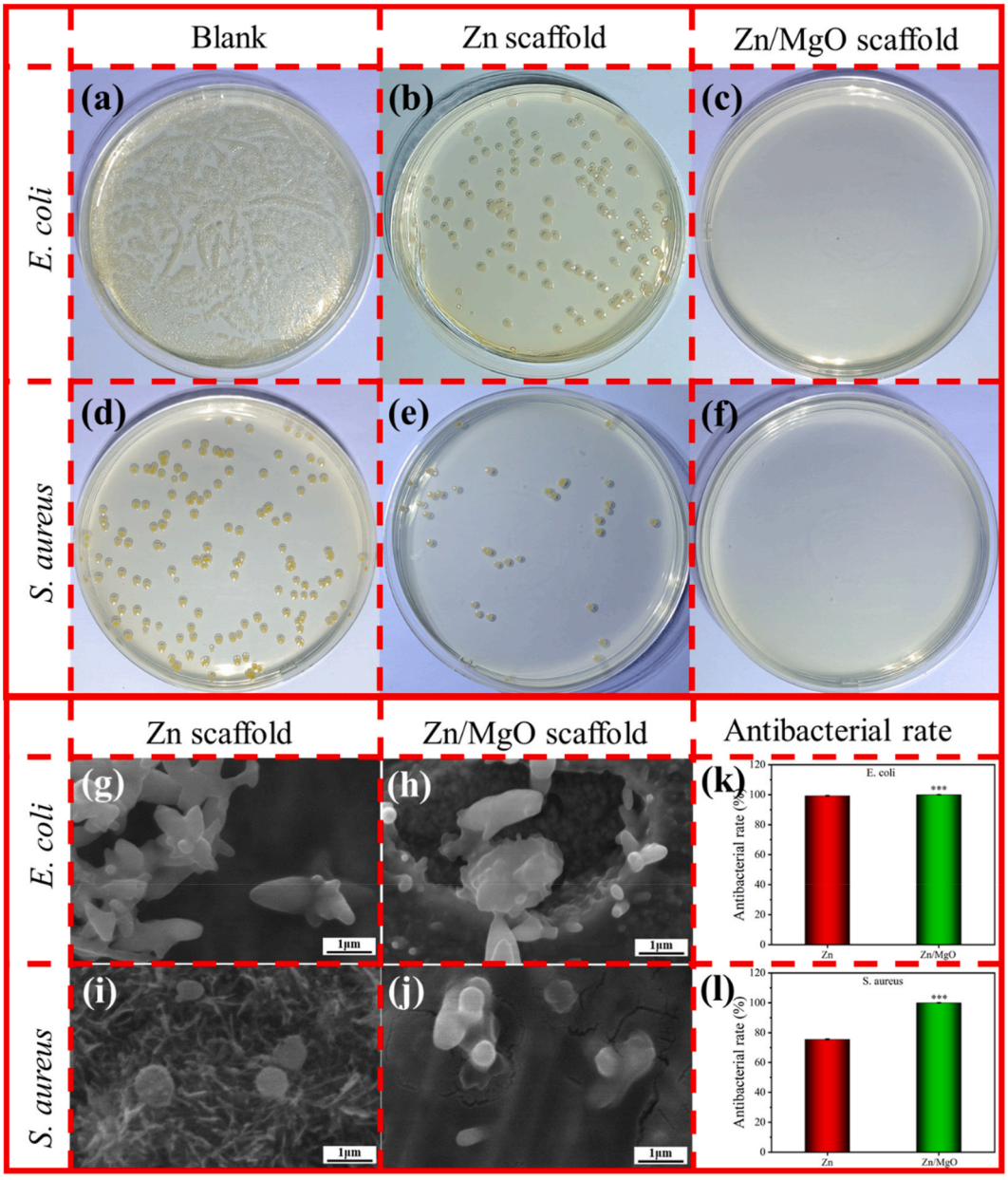

Fig. 4. Antibacterial susceptibility tests for *E. coli* and *S. aureus*. (a–f) Distribution of colonies on AGAR plates, (g–j) morphologies of bacteria on the surface of the pure Zn scaffold and the Zn/MgO composite scaffold when cocultured with bacterial solution for 24 h, (k–l) antibacterial rates of pure Zn scaffolds and Zn/MgO composite scaffolds against both bacteria (***$p < 0.001$).

3.5. In vitro biocompatibility

The adhesion behavior of adhesive cells usually determines their activity and function [49]. Fig. 5a–d shows the cell morphologies of the pure Zn scaffold and the Zn/MgO composite scaffold after coculture with MC-3T3 cells. On the untreated surface, the cells on the pure Zn scaffold and the Zn/MgO composite scaffold were nearly spherical, indicating that the cells had lost activity. On the pretreated surface, the cells on both the pure Zn scaffold and the Zn/MgO composite scaffold had pseudopods extending outward, indicating that the cells were in good condition. Compared with pure Zn scaffolds, Zn/MgO composite scaffolds showed more cell adhesion, better expansion and longer extension of pseudopods. This is due to the reaction of the scaffold with α-MEM to generate ZnO and $Zn(OH)_2$ during the in vitro pretreatment process, as well as the deposition of a small amount of Ca–P particles on the scaffold surface. These reasons led to the enhancement of the biocompatibility of the scaffold, and both cell adhesion and growth on the scaffold were enhanced. In addition, the number of adhered cells on the surface of the scaffolds indicates that the biocompatibility of Zn/MgO composite scaffolds is superior to that of pure Zn scaffolds. Fig. 5e-l indicate laser confocal scanning and staining photos of the adhesion of MC-3T3 cells on the surfaces of the pure Zn scaffold and the Zn/MgO composite scaffold. It was observed that numerous MC-3T3 cells adhered to the surfaces of the pure Zn scaffold and the Zn/MgO composite scaffold, and there were more cells on the surface of the Zn/MgO composite scaffold than on the surface of the pure Zn scaffold. Therefore, the Zn/MgO composite scaffolds showed better cytocompatibility and cell adhesion. The reason may be that MgO reacts with the culture medium to release Mg^{2+}, which activates PI3K/STAT7 through TRPM3 and enhances the proliferation and differentiation of osteoblasts by increasing the expression of osteoblast genes, thus promoting bone formation [50,51].

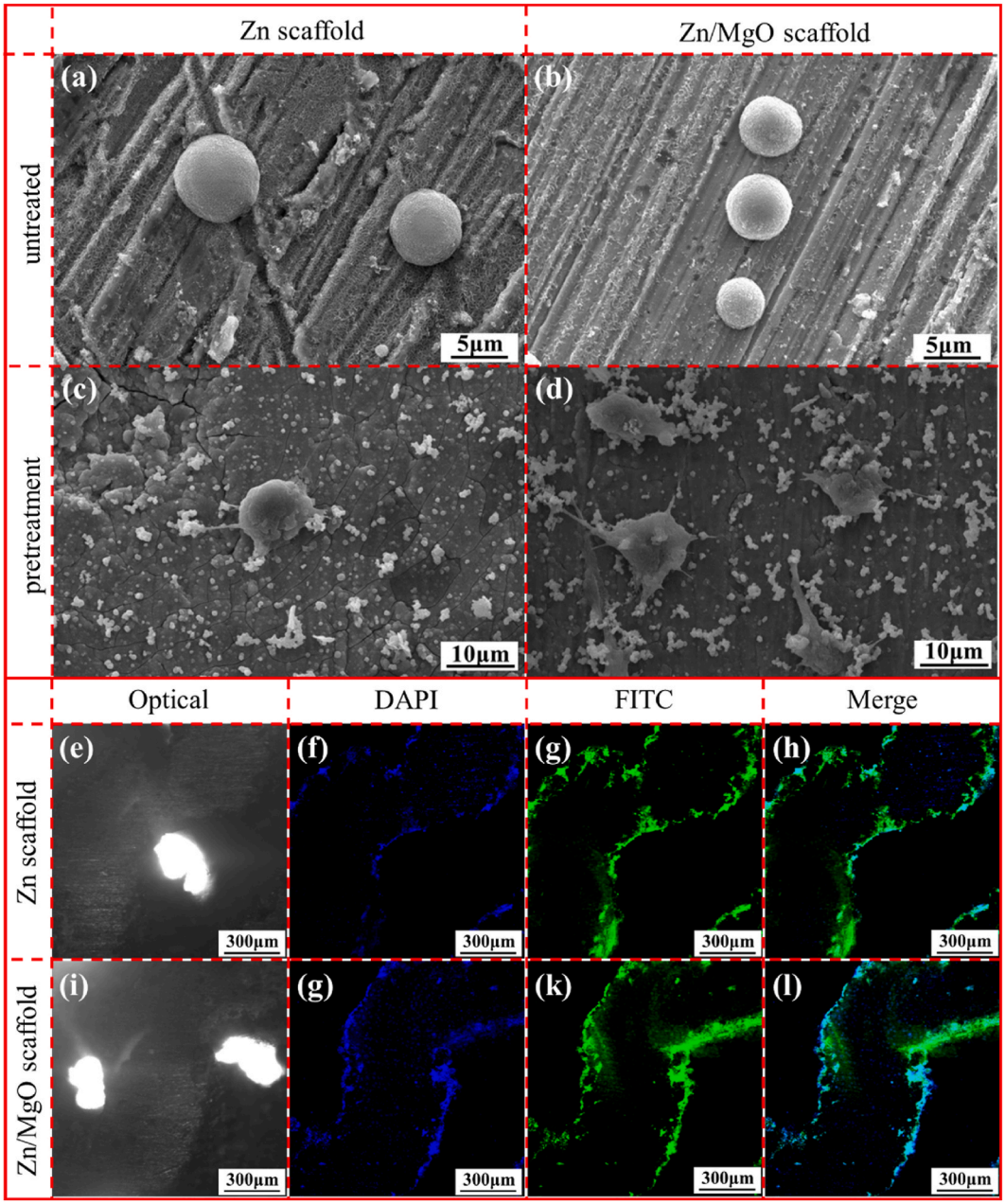

Fig. 5. In vitro biocompatibility of the scaffolds. (a–d) SEM images of the surface of the pure Zn scaffold and the Zn/MgO composite scaffold after coculture with MC-3T3 cells, (e–l) confocal laser mapping staining images of the adhesion of MC-3T3 cells on the surface of the pure Zn scaffold and the Zn/MgO composite scaffold.

3.6. In vivo implantation

Fig. 6a shows a general view of the SD rat skull defect model at different time points. It can be observed from Fig. 6a that the material surface of the Zn group and the Zn/MgO group showed newly formed bone-like tissue at 4 weeks. By 8 weeks and 12 weeks, a large amount of bone tissue was generated in both the Zn group and the Zn/MgO group. In the Zn/MgO group, more than half of the bone defect was covered by new bone tissue at 8 weeks and almost completely covered by new bone tissue at 12 weeks. In the Zn group, approximately half of the bone defect was covered by new bone tissue at 12 weeks. There was no obvious repair of bone defects in the blank group. These results indicated that Zn/MgO composite scaffolds had higher biocompatibility and osteogenic capacity than pure Zn scaffolds. Fig. 6b shows the quantitative analysis of the proportion of new bone tissue within a 5 mm diameter around the bone defect center by micro-CT calculation, denoted as BV/TV. There were significant differences between the Zn group and the Zn/MgO group at 4, 8 and 12 weeks, and the volume percentage by which the two scaffolds promoted the growth of new bone tissue increased with time. In addition, the percentage of new bone volume in the Zn/MgO group was significantly higher than that in the Zn group, indicating that Zn/MgO composite scaffolds had higher osteogenic capacity than pure Zn scaffolds. Fig. 6c indicates the remaining volume changes of the scaffolds at different implantation times. It is seen that the remaining volume of the pure Zn scaffold and Zn/MgO composite scaffold gradually decreased with time during the implantation process. The remaining volume of the pure Zn scaffold was about 90.8% and that of the Zn/MgO composite scaffold was about 84.4% at 12 weeks. It indicated that the degradation rate of Zn/MgO scaffolds was higher than that of pure Zn scaffolds. Fig. 6d shows the horizontal and sagittal images of the skull bone reconstructed by micro-CT, the scaffolds and the 3D models of the surrounding new bone. The surface of the two scaffolds was very smooth at 4 weeks after implantation. At 8 weeks, the surface of the scaffold became slightly rough, and at 12 weeks after implantation, the two scaffolds still had complete morphologies, and the surface roughness was increased. The degradation rates of both the pure Zn scaffold and the Zn/MgO composite scaffold were very slow. The amount of new bone tissue in the Zn group and the Zn/MgO group increased with time, and the new bone tissue became dense. As shown in Fig. 6e, Masson staining results of hard tissue sections of skull bone repair sites of SD rats at 4, 8 and 12 weeks were obtained. At 4 weeks, numerous of collagen fibers were observed around the scaffold of the Zn group, and a thin layer of discontinuous new bone-like tissue was observed around the scaffold. In the Zn/MgO group, a larger area and deeper staining of collagen fibers were observed around the scaffold than in the Zn group, and the amount of new bone-like tissues around the scaffold was higher than that in the Zn group. In the blank group, the bone defect contained a mixture of collagen fibers and muscle fibers, and no bone-like tissue was found. Collagen content and new bone tissue in the Zn/MgO group and the Zn group increased at 8 weeks compared with 4 weeks. In the Zn/MgO group, the new bone tissue was continuous, and the amount of new bone was significantly higher than that in the Zn group. There was a deep red-stained area near the Zn/MgO composite scaffold, which meant that mature bone tissue had appeared. No bone tissue was found in the blank group. At 12 weeks, the new bone tissue and collagen in the Zn/MgO group were further increased, to a much greater degree than in Zn group. There were new tissue connections on both sides of the pores of the scaffold. The new bone in the Zn group was discontinuous, thin, and had lower collagen content. The blank group showed numerous muscle fibers and no new bone formation. Therefore, the Zn/MgO group showed better osteogenic capacity in this study.

Studies [5] have shown that excessive Zn^{2+} in the body may have adverse effects on vital organs such as the kidneys, liver, spleen and heart. Therefore, HE staining was performed on the heart, liver, spleen, lung, and kidney of SD rats implanted in three groups both preimplantation (2 weeks) and postimplantation (12 weeks), and the results of the stained tissue sections are shown in Fig. S6. At 2 weeks and 12 weeks, there was no significant difference between the Zn group and the Zn/MgO group compared with the blank group, indicating that the pure Zn scaffold and the Zn/MgO composite scaffold both have good biocompatibility and no toxic side effects. Notably, some edema cells were observed in the liver tissue sections of the three groups at 12 weeks. By calculating the proportion of the number of edema cells in the total number of cells in the visual field (Fig. S7a), it was found that there was no significant difference between the blank group, the Zn group and the Zn/MgO group, so it was inferred that the edema cells had nothing to do with the implant materials. In addition, the blood routine of each SD rat at 2 weeks and 12 weeks was tested, and the results are shown in Figs. S7b–c. The total numbers of white blood cells, lymphocytes, monocytes and neutrophils in the preimplantation and postimplantation were all within the normal reference range, indicating that there was no inflammatory reaction preimplantation or postimplantation in SD rats, further confirming that the edema cells were not related to the implantation materials. Routine blood tests also confirmed that the pure Zn scaffold and the Zn/MgO composite scaffold have good biocompatibility in vivo.

4. Discussion

4.1. Effect of MgO nanoparticles on the degradation behavior of Zn/MgO composite scaffolds in SBF solution in vitro

As shown in Fig. 2d, the measured porosity and pore size of the pure Zn scaffolds and Zn/MgO composite scaffolds are very close to each other. While the corrosion rates of the two kinds of scaffolds shown in Fig. 3 are obviously different, and the incorporation of MgO nanoparticles changes the corrosion from pitting corrosion of pure Zn scaffolds to uniform corrosion of Zn/MgO composite scaffolds. It can be seen that porosity and pore size of the scaffolds are not the main factors affecting its degradation behavior, but the composition and microstructure of the scaffolds are the real root cause.

During the SLM preparation process, the rapid laser scanning and melt solidification can improve the microstructure of pure Zn scaffolds and Zn/MgO composite scaffolds, resulting in significant grain refinement [52,53]. As seen from the microstructure (Fig. 7a and b) and the average grain size (Fig. 7c) of the scaffolds, both of them show typical fast solidification microstructure characteristics. The microstructure of pure Zn scaffolds was denser, and the grain size distribution was different, with an average grain size of about 2.9 μm. Comparatively, the microstructure of Zn/MgO composite scaffolds showed a significant increase in small grains of 1–2 μm, and the average grain size decreased to about 2.1 μm. Obviously, the effect of MgO nanoparticles on the grain refinement of Zn matrix was not significant. From the SEM image and EDS analysis in Fig. 7d, the MgO nanoparticles were mainly distributed at the grain boundaries and they didn't play a role in promoting the heterogeneous nucleation of Zn matrix, which was directly related to the differences in the crystal structures and lattice constants of them. In general, the probability of forming interfaces between low-index crystal faces is much higher than that of high-index crystal faces [54]. Therefore, the closepacked faces (0001) of Zn matrix in Zn/MgO composites are most likely to form interfaces with the low-index crystal faces (001), (110) and (111) of MgO. According to Bramfitt's lattice mismatch theory [55], the goodness of the solidification interface is mainly determined by the atomic mismatch, and the interface with low atomic mismatch shows higher stability. The atomic mismatches (Supplementary materials) calculated from the lattice constants show that the mismatches of Zn(0001)/MgO(110) and Zn(0001)/MgO(100) are as high as 39.59% and 20.09%, respectively, which are far more than the mismatch limit of 12% for the formation of semicoherent interfaces. Furthermore, the mismatch of the most closepacked face Zn(0001)/MgO(111) between them is also close to 12%. As a result, the MgO nanoparticles could not

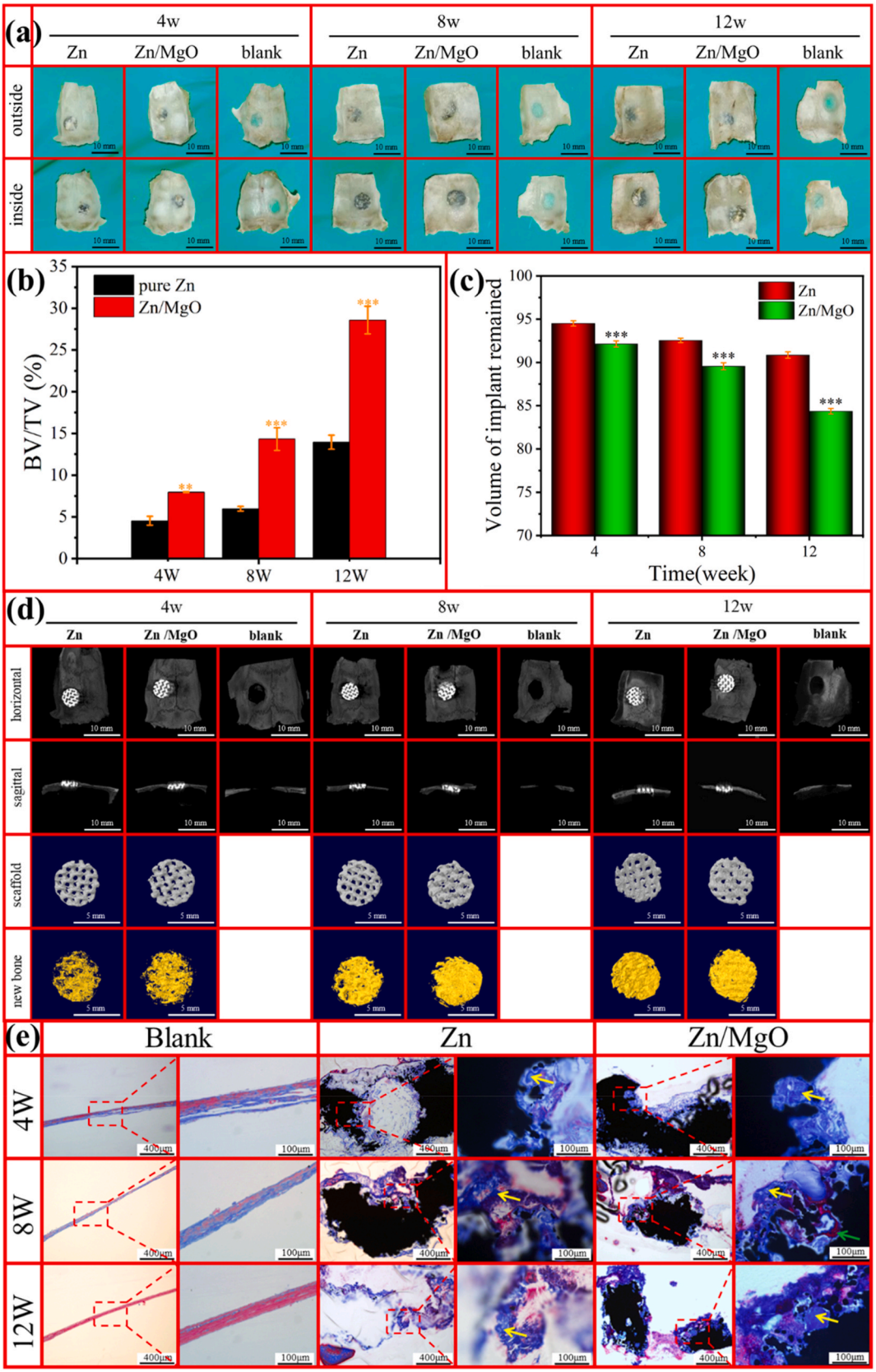

Fig. 6. In vivo biocompatibility of the scaffolds. (a) General view of the skull defect model at different time nodes, (b) percentage of new bone volume in the Zn group and the Zn/MgO group (**p < 0.01, ***p < 0.001), (c) horizontal and sagittal images of skull bone reconstructed by micro-CT, scaffolds and 3D models of surrounding new bone, (d) Masson staining results of hard tissue sections of the skull bone repair sites of SD rats at 4, 8 and 12 weeks, the red box is the selected field of view for further observation (yellow arrows are new bone tissue, and green arrows are mature bone tissue).

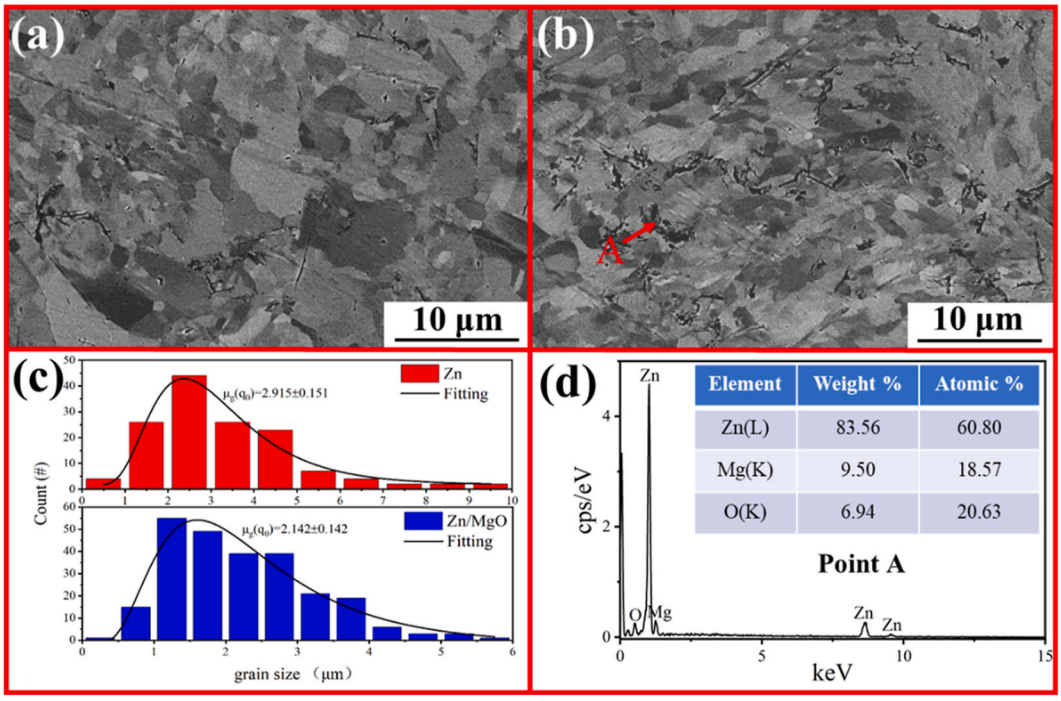

Fig. 7. The microstructure and average grain size of the scaffolds. (a) Backscattering SEM image of the pure Zn scaffold, (b) backscattering SEM image of the Zn/MgO composite scaffold, (c) average grain size of scaffolds, (d) the EDS analysis at point A.

be the core of the heterogeneous nucleation of the Zn matrix or form a good interfacial bond with the Zn matrix. These MgO nanoparticles were pushed to the grain boundaries at the end of solidification, which played a certain role in refining the grains, but also increased the number of micropores in the solid near the grain boundaries, which made the density of the solid part of the Zn/MgO composite scaffolds (Fig. 2e) lower than that of the pure Zn scaffolds.

It is the addition of MgO nanoparticles and their weak interfacial bonding with the Zn matrix that leads to certain changes in the degradation behavior and corrosion mechanisms of both scaffolds in SBF solution. According to literature [56], the following chemical reactions occur when the exposed Zn matrix comes into contact with SBF solution.

$$Zn \rightarrow Zn^{2+} + 2e^{-} \text{ Anode reaction} \quad (3)$$

$$O_2 + 4e^{-} + 2H_2O \rightarrow 4OH^{-} \text{ Cathode reaction} \quad (4)$$

$$2Zn + O_2 + 2H_2O \rightarrow 2Zn(OH)_2 \text{ Total reaction} \quad (5)$$

$$Zn(OH)_2 \rightarrow ZnO + H_2O \text{ Subsequent reaction} \quad (6)$$

In the anode reaction, Zn loses electrons, and in the cathode reaction, O_2 gains electrons. The total reaction results in a $Zn(OH)_2$ product, which in a subsequent reaction is converted to ZnO and H_2O. Cl^{-} in SBF solution can convert insoluble ZnO into soluble chloride salts [56,57]. After that, the Zn matrix is then exposed to SBF solution and continues to undergo corrosive degradation in reaction (5). During the series of reactions, the pure Zn scaffold completed its own degradation process. As shown from Fig. 3, during the corrosion reaction, the ion exchange at the angular position of the pure Zn scaffold is the fastest, meanwhile, the lack of protection by Ca–P products makes the pure Zn scaffold tend to local corrosion in the concentrated area. Therefore, after 30 days of immersion, the corners of the pure Zn scaffolds were detached in large pieces, and the corrosion rate was significantly increased caused by uneven corrosion, which was very likely to lead to premature failure of the pure Zn scaffolds.

Compared with the localized severe corrosion of pure Zn scaffolds, the Zn/MgO composite scaffolds exhibited uniform degradation behavior when in contact with SBF solution. The average corrosion rate within 10 days of in vitro immersion increased by 0.5 mg/day compared with that of pure Zn scaffolds, but decreased significantly at the later stage of immersion. The change of pH value of SBF solution with immersion time also showed the same pattern of change (Fig. 3i). The analyzed reasons may be attributed to the following points. (1) The high chemical activity of MgO nanoparticles in Zn/MgO composite scaffolds that were deviated at the grain boundaries might preferentially react with Cl^{-} and H_2O in the SBF solution to release Mg^{2+} and OH^{-} (reaction 7), and consequently induced the deposition of Ca^{2+} and PO3- 4 at the grain boundaries in the SBF solution. Moreover, the MgO nanoparticles were more uniformly distributed throughout the scaffold, causing the Zn/MgO composite scaffolds to degrade by uniform corrosion at the beginning in SBF solution. (2) Only an incoherent interface could be formed between MgO nanoparticles and Zn matrix in Zn/MgO composite scaffolds, and the atomic arrangement density was relatively reduced. The SBF solution would preferentially penetrate inward from their interfaces, preferentially corroded the MgO particles distributed on the grain boundary of the next layer, and uniformly corroded and degraded inward layer by layer. (3) Corrosion shedding of MgO nanoparticles from the surface layer of Zn/MgO composite scaffolds made the surface area of the scaffolds larger, which also increased the progression of a series of reactions (3–6) in the Zn matrix, thus accelerating the corrosion rate. (4) Grain boundaries had higher energy and were more chemically active. Thus, high-density grain boundaries increased the surface reactivity of the sample by increasing electronic activity and diffusion [58] and led to the rapid formation of a uniform and dense protective layer [59,60]. Obviously, the fine grain size of Zn/MgO composite scaffolds also contributed to their increased corrosion rate in the early period. (5) With the continuous corrosion of the MgO nanoparticles in the Zn/MgO composite scaffolds and the uniform degradation of the Zn matrix, a large amount of Ca–P products were continuously deposited on the surface of the Zn/MgO composite scaffolds. The accumulation of Ca–P products during 10–30 days of immersion might block the pores of the scaffolds and hinder the effective contact between the SBF solution and the scaffolds, thus causing the corrosion rate of the Zn/MgO composite scaffolds to be significantly lower than that of the pure Zn scaffolds. However, this paradoxical

phenomenon was mainly attributed to the relatively static corrosion pattern in vitro. The relatively static degradation experiments are more meaningful for the evaluation of the porous scaffolds during the early immersion period.

$$MgO + H_2O \xrightarrow{Cl^-} Mg^{2+} + 2OH^- \quad (7)$$

In general, the pure Zn scaffold and the Zn/MgO composite scaffold in this study showed good in vitro degradation behavior when immersed in SBF solution. The maximum corrosion rate of the scaffolds calculated from weight loss was 4.6 mg/day, which was far lower than the limit of daily Zn intake of the human body (40 mg/day) [61].

4.2. *Effect of MgO nanoparticles on the degradation behavior in vivo and biocompatibility of Zn/MgO composite scaffolds*

Good biocompatibility is a prerequisite for the orthopedic application of biomaterials [62] and an important factor to be considered for metallic biomaterials. In this study, 3D-printed pure Zn scaffolds and Zn/MgO composite scaffolds were co-cultured with MC-3T3 cells to study in vitro biocompatibility, respectively, and both scaffolds were implanted into the cranial defects in SD rats to study in vivo biocompatibility. As shown in Fig. 5, a large number of MC-3T3 cells were adhered to the surface and pore walls of the scaffolds after 48 h of co-culture with MC-3T3 cells in vitro for both pure Zn scaffolds and Zn/MgO composite scaffolds, and the density of MC-3T3 cells in Zn/MgO composite scaffolds was significantly higher than that in pure Zn scaffolds. It indicated that the addition of MgO nanoparticles enhanced the histocompatibility of Zn scaffolds, in which the microenvironment created by preferential corrosion of MgO nanoparticles was more favorable for the adsorption, propagation and growth of cells on the scaffolds and within their pores. This is due to the fact that MgO nanoparticles can generate Mg^{2+} during degradation. And Mg^{2+} is a versatile and therapeutic ion in promoting cell migration, proliferation, and angiogenesis [63]. When the scaffolds were implanted into the cranial defects of SD rats, the same effect was seen from around the scaffold and its guidance of new bone growth within a period of 12 weeks (Fig. 6). A large amount of new bone tissue was observed to grow into the pores at 4 w and 8 w for both scaffolds, and the amount of new bone regeneration increased with the increase of implantation time. However, it is easily seen from the quantitative new bone calculations (Fig. 6b) that the Zn/MgO composite scaffolds guided the amount of new bone regeneration was consistently significantly higher than that of the pure Zn scaffolds. At 12 w, the amount of new bone tissue (BV/TV) in the pores of Zn/MgO composite scaffolds had been up to nearly 30%, while that of Zn scaffolds was less than 15%. It was well demonstrated that the Zn/MgO composite scaffolds had more excellent biocompatibility and promoting osteogenic activity in vivo. This indicated that the addition of MgO nanoparticles was very helpful for the improvement of the biocompatibility of Zn scaffolds. The reason is that the Mg^{2+} generated by the degradation of MgO nanoparticles through reactions (7) could improve the proliferation and adhesion of human bone-derived cells [64], thus accelerating bone healing in the bone defect site. A schematic diagram of new bone tissue growing into the scaffold pores is shown in Fig. 8. When the scaffold comes in contact with body fluid, the scaffold will undergo degradation. Ca^{2+}, OH^- and PO3- 4 in body fluid react on the surface of the Zn matrix to generate a Ca–P product layer, which has good biocompatibility and benefits the adhesion of osteoblasts. Osteoblasts arranges and connects under the promotion of Zn^{2+}, and eventually form bone trabeculae. The pore structure of the scaffolds will guide the growth of new bone tissue. The generation of Mg^{2+} will synergistically promote the growth of new bone tissue with Zn^{2+}, resulting in a higher rate of induction of new bone tissue and amount of generating bone trabeculae in the Zn/MgO scaffold than in the Zn scaffold. Although the Zn/MgO composite scaffolds exhibited a faster degradation behavior in the early stage and a slower degradation behavior in the late stage compared to the pure Zn scaffolds during the relatively static corrosion process in vitro, the remaining volume of the Zn/MgO composite scaffolds was consistently lower than that of the pure Zn scaffolds as shown in Fig. 6c at different implantation times. Especially after 12 w of implantation, the remaining volume of the Zn/MgO composite

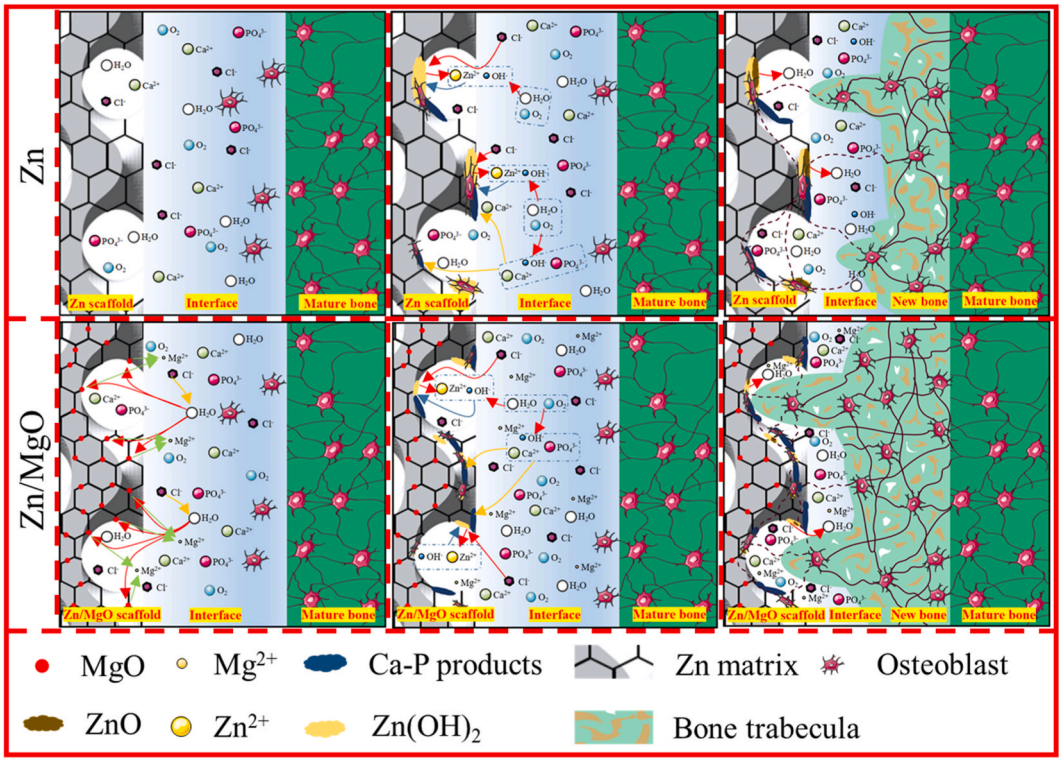

Fig. 8. The degradation mechanism and guiding new bone regeneration of the pure Zn scaffold and the Zn/MgO composite scaffold.

scaffolds was 84.4%. Whereas in the studies of Ren et al. [65] and Xia et al. [66], the remaining volume of infiltration casting pure Zn and Zn–2Cu scaffolds at 6 months of in vivo implantation was 86.9% and 82.9%, and that of 3D-printed Diamond-structured pure Zn scaffolds at 6 months of in vivo implantation was 91%. This fully demonstrates that the regulation of the degradation behavior of Zn scaffolds by MgO nanoparticles in vivo is very effective.

5. Conclusion

In this study, a layer of bioactive MgO nanoparticles was wrapped on the surface of spherical Zn powder by ball milling treatment, which allowed the incorporation of MgO nanoparticles into Zn matrix by 3D printing. The microstructure, mechanical properties, degradation behavior, antibacterial properties, and in vitro and in vivo biocompatibility of porous Zn and Zn/MgO scaffolds were systematically investigated. The main findings are summarized as follows.

1. MgO nanoparticles refined the microstructure of Zn/MgO composite scaffolds and improved the hardness of Zn matrix. The yield strength values of both the pure Zn scaffold and the Zn/MgO composite scaffold were within the typical compressive strength range of cancellous bone;
2. The incorporation of MgO nanoparticles can regulate the corrosion rate of Zn matrix, which makes the corrosion degradation behavior of Zn/MgO composite scaffolds in SBF solution more uniform. The maximum weight loss rate (4.6 mg/day) was far lower than the limit of daily Zn intake of the human body (40 mg/day);
3. The Zn/MgO composite scaffolds with added MgO nanoparticles had excellent in vitro and in vivo biocompatibility, which showed better ability to guide bone tissue regeneration in rat cranial bone repair experiments compared with pure Zn scaffolds. In addition, both pure Zn and Zn/MgO scaffolds did not affect the organs and blood of rats.
4. Both pure Zn and Zn/MgO scaffolds had good antibacterial effects, and the antibacterial rate of Zn/MgO composite scaffolds was higher than that of pure Zn scaffolds, which indicated that both Zn ions and MgO nanoparticles could inhibit bacterial adhesion and biofilm formation.
5. In order to further improve the property of Zn/MgO composite scaffolds, future work could focus on the study of 3D printing parameters, incorporation content of MgO nanoparticles, and the simulation of the body fluid flow in the scaffold implant and the changing trend of mechanical properties with time. This work will lead to wider and deeper research towards practical applications in the field of materials science and bone tissue engineering.

Ethics approval and consent to participate

All animal procedures were performed with the Guidelines for the Care and Use of Laboratory Animals of Tianjin Medical University in China and approved by the Animal Ethics Committee of Tianjin Medical University (Tianjin, China, SYXK 2019-0004).

Declaration of interests

Yufeng Zheng is an editor-in-chief for Bioactive Materials and was not involved in the editorial review or the decision to publish this article. All authors declare that there are no competing interests.

CRediT authorship contribution statement

Leiting Yu: Writing – review & editing, Writing – original draft, Visualization, Methodology, Investigation, Formal analysis, Data curation, Conceptualization. **Fengdong Sun:** Writing – original draft, Methodology, Investigation, Formal analysis. **Yuanyuan Wang:** Methodology, Investigation. **Wei Li:** Investigation, Funding acquisition, Formal analysis. **Yufeng Zheng:** Supervision. **Guangxin Shen:** Formal analysis. **Yao Wang:** Writing – review & editing, Supervision, Funding acquisition. **Minfang Chen:** Writing – review & editing, Supervision, Funding acquisition, Conceptualization.

Acknowledgements

The authors acknowledge the financial support for this work from the National Natural Science Foundation of China (Nos. 52171241 and 52373251).

The authors acknowledge the printing work provided by Xi'An Bright Laser Technologies Co., Ltd.

Tianjin University of Technology Graduate Research Innovation Project.

Appendix A. Supplementary data

Supplementary data to this article can be found online at https://doi.org/10.1016/j.bioactmat.2024.03.016.

References

[1] J. Zhang, Y. Jiang, Z. Shang, et al., Biodegradable metals for bone defect repair: a systematic review and meta-analysis based on animal studies, Bioact. Mater. 6 (2021) 4027–4052, https://doi.org/10.1016/j.bioactmat.2021.03.035.
[2] S. Agarwal, J. Curtin, B. Duffy, et al., Biodegradable magnesium alloys for orthopaedic applications: a review on corrosion, biocompatibility and surface modifications, Mater. Sci. Eng. C 68 (2016) 948–963, https://doi.org/10.1016/j.msec.2016.06.020.
[3] A.J. Drelich, S. Zhao, R.J. Guillory, et al., Long-term surveillance of zinc implant in murine artery: surprisingly steady biocorrosion rate, Acta Biomater. 58 (2017) 539–549, https://doi.org/10.1016/j.actbio.2017.05.045.
[4] L. Rink, P. Gabriel, Zinc and the immune system, Proc. Nutr. Soc. 59 (2000) 541–552, https://doi.org/10.1017/s0029665100000781.
[5] J.M. Berg, Y. Shi, The galvanization of biology: a growing appreciation for the roles of zinc, Science 271 (1996) 1081–1085, https://doi.org/10.1126/science.271.5252.1081.
[6] H. Tapiero, K.D. Tew, Trace elements in human physiology and pathology: zinc and metallothioneins, Biomed. Pharmacother. 57 (2003) 399–411, https://doi.org/10.1016/S0753-3322(03)00081-7.
[7] J. He, D. Li, F. He, et al., A study of degradation behaviour and biocompatibility of Zn-Fe alloy prepared by electrodeposition, Mater. Sci. Eng. C 117 (2020) 111295, https://doi.org/10.1016/j.msec.2020.111295.
[8] P. Wen, Y. Qin, Y. Chen, et al., Laser additive manufacturing of Zn porous scaffolds: shielding gas flow, surface quality and densification, J. Mater. Sci. Technol. 2 (2019) 368–376, https://doi.org/10.1016/j.jmst.2018.09.065.
[9] Y. Su, I. Cockerill, Y. Wang, et al., Zinc-based biomaterials for regeneration and therapy, Trends Biotechnol. 37 (2019) 428–441, https://doi.org/10.1016/j.tibtech.2018.10.009.
[10] C.J. Frederickson, J.Y. Koh, A. Bush, The neurobiology of zinc in health and disease, Nat. Rev. Neurosci. 6 (2005) 449–462, https://doi.org/10.1038/nrn1671.
[11] W. Zhang, P. Li, B. Neumann, et al., Chandler-Loop surveyed blood compatibility and dynamic blood triggered degradation behavior of Zn-4Cu alloy and Zn, Mater. Sci. Eng. C 119 (2021) 111594, https://doi.org/10.1016/j.msec.2020.111594.
[12] Y. Yin, C. Zhou, Y. Shi, et al., Hemocompatibility of biodegradable Zn-0.8 wt% (Cu, Mn, Li) alloys, Mater. Sci. Eng. C 104 (2019) 109896, https://doi.org/10.1016/j.msec.2019.109896.
[13] Y. Zhang, J. Xu, Y. Ruan, et al., Implant-derived magnesium induces local neuronal production of CGRP to improve bone-fracture healing in rats, Nat. Med. 22 (2016) 1160–1169, https://doi.org/10.1038/nm.4162.
[14] Z. Tang, H. Huang, J. Niu, et al., Design and characterizations of novel biodegradable Zn-Cu-Mg alloys for potential biodegradable implants, Mater. Des. 117 (2017) 84–94, https://doi.org/10.1016/j.matdes.2016.12.075.
[15] H. Li, X. Xie, Y. Zheng, et al., Development of biodegradable Zn-1X binary alloys with nutrient alloying elements Mg, Ca and Sr, Sci. Rep. 5 (2015) 10719, https://doi.org/10.1038/srep10719.
[16] F. Witte, N. Hort, C. Vogt, et al., Degradable biomaterials based on magnesium corrosion, Curr. Opin. Solid State Mater. Sci. 12 (2008) 63–72, https://doi.org/10.1016/j.cossms.2009.04.001.
[17] D. Vojtěch, J. Kubásek, J. Šerák, et al., Mechanical and corrosion properties of newly developed biodegradable Zn-based alloys for bone fixation, Acta Biomater. 7 (2011) 3515–3522, https://doi.org/10.1016/j.actbio.2011.05.008.
[18] G. Li, H. Yang, Y. Zheng, et al., Challenges in the use of zinc and its alloys as biodegradable metals: perspective from biomechanical compatibility, Acta Biomater. 97 (2019) 23–45, https://doi.org/10.1016/j.actbio.2019.07.038.
[19] Y. Zheng, X. Gu, F. Witte, Biodegradable metals, Mater. Sci. Eng. R 77 (2014) 1–34, https://doi.org/10.1016/j.mser.2014.01.001.
[20] P. Guo, X. Zhu, L. Yang, et al., Ultrafine- and uniform-grained biodegradable Zn-0.5Mn alloy: grain refinement mechanism, corrosion behavior, and

biocompatibility in vivo, Mater. Sci. Eng. C 118 (2021) 111391, https://doi.org/10.1016/j.msec.2020.111391.
[21] S.Z. Khalajabadi, M.R.A. Kadir, S. Izman, et al., The effect of MgO on the biodegradation, physical properties and biocompatibility of a Mg/HA/MgO nanocomposite manufactured by powder metallurgy method, J. Alloys Compd. 655 (2016) 266–280, https://doi.org/10.1016/j.jallcom.2015.09.107.
[22] S. Sahmani, S. Saber-Samandari, A. Khandan, et al., Influence of MgO nanoparticles on the mechanical properties of coated hydroxyapatite nanocomposite scaffolds produced via space holder technique: fabrication, characterization and simulation, J. Mech. Behav. Biomed. Mater. 95 (2019) 76–88, https://doi.org/10.1016/j.jmbbm.2019.03.014.
[23] R. Yao, Y. Zhao, S. Han, et al., Microstructure, mechanical properties, in vitro degradation behavior and in vivo osteogenic activities of Zn-1Mg-β-TCP composites for bone defect repair, Mater. Des. 225 (2023) 111494, https://doi.org/10.1016/j.matdes.2022.111494.
[24] C. Pan, X. Sun, G. Xu, et al., The effects of β-TCP on mechanical properties, corrosion behavior and biocompatibility of β-TCP/Zn-Mg composites, Mater. Sci. Eng. C 108 (2020) 110397, https://doi.org/10.1016/j.msec.2019.110397.
[25] G. Lu, G. Xu, B. Helian, et al., Fabrication and properties of a biodegradable β-TCP/Zn-Mg bio-composite, Mater. Res. Express (2019) 6, https://doi.org/10.1088/2053-1591/ab2861.
[26] T. Lei, C. Ouyang, W. Tang, et al., Enhanced corrosion protection of MgO coatings on magnesium alloy deposited by an anodic electrodeposition process, Corrosion Sci. 52 (2010) 3504–3508, https://doi.org/10.1016/j.corsci.2010.06.028.
[27] C. Tang, S. Lyu, Z. Zhao, et al., Effects of MgO nano particles on the mechanical properties and corrosion behavior of Mg-Zn-Ca alloy, Mater. Chem. Phys. 297 (2023) 127380, https://doi.org/10.1016/j.matchemphys.2023.127380.
[28] C.S. Goh, M. Gupta, J. Wei, et al., Characterization of high performance Mg/MgO nanocomposites, J. Compos. Mater. 41 (2007) 2325–2335, https://doi.org/10.1177/0021998307075445.
[29] S.Z. Khalajabadi, M.R.A. Kadir, S. Izman, et al., Fabrication, bio-corrosion behavior and mechanical properties of a Mg/HA/MgO nanocomposite for biomedical applications, Mater. Des. 88 (2015) 1223–1233, https://doi.org/10.1016/j.matdes.2015.09.065.
[30] Y.N. Kumar, B. Venkateswarlu, L.R. Raju, et al., Developing Zn-MgO composites for degradable implant applications by powder metallurgy route, Mater. Lett. 302 (2021) 130433, https://doi.org/10.1016/j.matlet.2021.130433.
[31] S. Ma, K. Song, J. Lan, et al., Biological and mechanical property analysis for designed heterogeneous porous scaffolds based on the refined TPMS, J. Mech. Behav. Biomed. Mater. 107 (2020) 103727, https://doi.org/10.1016/j.jmbbm.2020.103727.
[32] A. Ataee, Y. Li, D. Fraser, et al., Anisotropic Ti-6Al-4V gyroid scaffolds manufactured by electron beam melting (EBM) for bone implant applications, Mater. Des. 137 (2018) 345–354, https://doi.org/10.1016/j.matdes.2017.10.040.
[33] G. Lin, D. Liu, M. Chen, et al., Preparation and characterization of biodegradable Mg-Zn-Ca/MgO nanocomposites for biomedical applications, Mater. Char. 144 (2018) 120–130, https://doi.org/10.1016/j.matchar.2018.06.028.
[34] Y. Li, P. Pavanram, J. Zhou, et al., Additively manufactured biodegradable porous zinc, Acta Biomater. 101 (2020) 609–623, https://doi.org/10.1016/j.actbio.2019.10.034.
[35] G. Jiang, G. He, A new approach to the fabrication of porous magnesium with well-controlled 3D pore structure for orthopedic applications, Mater. Sci. Eng. C 43 (2014) 317–320, https://doi.org/10.1016/j.msec.2014.07.033.
[36] A.A. Zadpoor, Mechanical performance of additively manufactured meta-biomaterials-ScienceDirect, Acta Biomater. 85 (2019) 41–59, https://doi.org/10.1016/j.actbio.2018.12.038.
[37] I. Cockerill, Y. Su, S. Sinha, et al., Porous zinc scaffolds for bone tissue engineering applications: a novel additive manufacturing and casting approach, Mater. Sci. Eng. C 110 (2020) 10738, https://doi.org/10.1016/j.msec.2020.110738.
[38] W. Jiang, J. Wang, Q. Liu, et al., Low hydrogen release behavior and antibacterial property of Mg-4Zn-xSn alloys, Mater. Lett. 241 (2019) 88–91, https://doi.org/10.1016/J.MATLET.2019.01.048.
[39] L. Yu, S. Lyu, Y. Chen, et al., Simultaneously improving the mechanical property and corrosion resistance of extruded biomedical Mg-3Zn alloy by forming in-situ MgO, J. Mater. Res. Technol. 18 (2022) 2977–2992, https://doi.org/10.1016/j.jmrt.2022.03.173.
[40] C. Yan, L. Hao, A. Hussein, et al., Advanced lightweight 316L stainless steel cellular lattice structures fabricated via selective laser melting, Mater. Des. 55 (2014) 533–541, https://doi.org/10.1016/j.matdes.2013.10.027.
[41] K. Chua, I. Khan, R. Malhotra, et al., Additive manufacturing and 3D printing of metallic biomaterials, Engineered Regeneration 2 (2021) 288–299, https://doi.org/10.1016/j.engreg.2021.11.002.
[42] S. Wu, X. Liu, K.W.K. Yeung, et al., Biomimetic porous scaffolds for bone tissue engineering, Mater. Sci. Eng. R 80 (2014) 1–36, https://doi.org/10.1016/j.mser.2014.04.001.
[43] T.M. Keaveny, E.F. Morgan, G.L. Niebur, et al., Biomechanics of trabecular bone, Annu. Rev. Biomed. Eng. 3 (2001) 307–333, https://doi.org/10.1146/annurev.bioeng.3.1.307.
[44] C.J. Hernandez, G.S. Beaupré, T.S. Keller, et al., The influence of bone volume fraction and ash fraction on bone strength and modulus, Bone 29 (2001) 74–78, https://doi.org/10.1016/s8756-3282(01)00467-7.
[45] F.P.W. Melchels, K. Bertoldi, R. Gabbrielli, et al., Mathematically defined tissue engineering scaffold architectures prepared by stereolithography, Biomaterials 31 (2010) 6909–6916, https://doi.org/10.1016/j.biomaterials.2010.05.068.
[46] S.M. Dizaj, F. Lotfipour, M. Barzegar-jalali, et al., Antimicrobial activity of the metals and metal oxide nanoparticles, Mater. Sci. Eng. C 44 (2014) 278–284, https://doi.org/10.1016/j.msec.2014.08.031.
[47] H.R. Raveesha, S. Nayana, D.R. Vasudha, et al., The electrochemical behavior, antifungal and cytotoxic activities of phytofabricated MgO nanoparticles using Withania somnifera leaf extract, J. Sci.: Advanced Materials and Devices 4 (2019) 57–65, https://doi.org/10.1016/j.jsamd.2019.01.003.
[48] N. Aničić, M. Vukomanović, D. Suvorov, The nano-texturing of MgO microrods for antibacterial applications, RSC Adv. 6 (2016) 102657–102664, https://doi.org/10.1039/c6ra23058j.
[49] X. Zhang, H. Yin, L. Xiao, et al., Chitosan regulated electrochemistry for dense hydroxyapatite/MgO nanocomposite coating with antibiosis and osteogenesis on titanium alloy, Colloid and Interface Science Communications 48 (2022) 100616, https://doi.org/10.1016/j.colcom.2022.100616.
[50] X. Zhang, H. Zu, D. Zhao, et al., Ion channel functional protein kinase TRPM7 regulates mg ions to promote the osteoinduction of human osteoblast via PI3K pathway: in vitro simulation of the bone-repairing effect of mg-based alloy implant, Acta Biomater. 63 (2017) 369–382, https://doi.org/10.1016/j.actbio.2017.08.051.
[51] J. Wang, X. Ma, Y. Feng, et al., Magnesium ions promote the biological behaviour of rat calvarial osteoblasts by activating the PI3K/Akt signalling pathway, Biol. Trace Elem. Res. 179 (2017) 284–293, https://doi.org/10.1007/s12011-017-0948-8.
[52] Y. Li, X. Yao, S. Cao, et al., Rapidly solidified and optimally constraint-aged Ni51Ti49 shape memory alloy aiming at making a purpose-designed bio-actuator, Mater. Des. 118 (2017) 99–106, https://doi.org/10.1016/j.matdes.2017.01.001.
[53] C. Shuai, Y. Yang, P. Wu, et al., Laser rapid solidification improves corrosion behavior of Mg-Zn-Zr alloy, J. Alloys Compd. 691 (2017) 961–969, https://doi.org/10.1016/j.jallcom.2016.09.019.
[54] L.Z. Mezey, W. Hofer, An improved thermodynamic calculation of interface properties and its application for low-index and polycrystalline surfaces of PtNi, Surf. Sci. 269–270 (1992) 1135–1141, https://doi.org/10.1016/0039-6028(92)91405-Z.
[55] B.L. Bramfitt, The effect of carbide and nitride additions on the heterogeneous nucleation behavior of liquid iron, Metall. Mater. Trans. B 1 (1970) 1987–1995, https://doi.org/10.1007/BF02642799.
[56] X. Liu, J. Sun, K. Qiu, et al., Effects of alloying elements (Ca and Sr) on microstructure, mechanical property and in vitro corrosion behavior of biodegradable Zn-1.5Mg alloy, J. Alloys Compd. 664 (2016) 444–452, https://doi.org/10.1016/j.jallcom.2015.10.116.
[57] W. Feitknecht, Studies on the influence of chemical factors on the corrosion of metals, Chem. Ind. 36 (1959) 1102–1109.
[58] W.R. Osorio, C.M.D.A. Freire, A. Garcia, The role of macrostructural morphology and grain size on the corrosion resistance of Zn and Al castings, Mater. Sci. Eng., A 402 (2005) 22–32, https://doi.org/10.1016/j.msea.2005.02.094.
[59] E. Kus, Z. Lee, S.R. Nutt, et al., A comparison of the corrosion behavior of nanocrystalline and conventional Al 5083 samples, Corrosion 62 (2006) 152–161, https://doi.org/10.5006/1.3278260.
[60] M.K. Chung, Y. Choi, J.G. Kim, et al., Effect of the number of ECAP pass time on the electrochemical properties of 1050 Al alloys, Mater. Sci. Eng., A 366 (2004) 282–291, https://doi.org/10.1016/j.msea.2003.08.056.
[61] Y. Xie, L. Zhao, Z. Zhang, et al., Fabrication and properties of porous Zn-Ag alloy scaffolds as biodegradable materials, Mater. Chem. Phys. 219 (2018) 433–443, https://doi.org/10.1016/j.matchemphys.2018.08.023.
[62] J. He, F. Xu, R. Dong, et al., Electrohydrodynamic 3D printing of microscale poly (ε-caprolactone) scaffolds with multi-walled carbon nanotubes, Biofabrication 9 (2017) 015007, https://doi.org/10.1088/1758-5090/aa53bc.
[63] Z.Y. Yuan, Z. Wan, C.Y. Gao, et al., Controlled magnesium ion delivery system for in situ bone tissue engineering, J. Contr. Release 350 (2022) 360–376, https://doi.org/10.1016/j.jconrel.2022.08.036.
[64] H. Zreiqat, C.R. Howlett, A. Zannettino, et al., Mechanisms of magnesium-stimulated adhesion of osteoblastic cells to commonly used orthopaedic implants, J. Biomed. Mater. Res. 62 (2002) 175–184, https://doi.org/10.1002/jbm.10270.
[65] H. Ren, C. Pan, Y. Liu, et al., Fabrication, in vitro and in vivo properties of porous Zn–Cu alloy scaffolds for bone tissue engineering, Mater. Chem. Phys. 289 (2022) 126458, https://doi.org/10.1016/j.matchemphys.2022.126458.
[66] D. Xia, Y. Qin, H. Guo, et al., Additively manufactured pure zinc porous scaffolds for critical-sized bone defects of rabbit femur, Bioact. Mater. 19 (2023) 12–23, https://doi.org/10.1016/j.bioactmat.2022.03.010.